Two-Dimensional SnS2 Nanosheets Exfoliated from Inorganic-Organic Hybrid with Enhanced Photocatalytic Activity towards Cr(VI) Reduction

Journal:	*Inorganic Chemistry Frontiers*
Manuscript ID	QI-RES-01-2019-000020.R1
Article Type:	Research Article
Date Submitted by the Author:	07-Feb-2019
Complete List of Authors:	Liu, Yongping; Guilin University of Technology, College of Chemical and Bioengineering Mi, Xihong; Guilin University of Technology, College of Chemical and Bioengineering Wang, Jixiang; Guilin University of Technology, College of Chemical and Bioengineering Li, Ming; Guilin University of Technology, College of Chemical and Biologic Engineering Fan, Dayong; Guilin University of Technology, College of Chemistry and Bioengineering Lu, Huidan; Guilin University of Technology, College of Chemical and Bioengineering Chen, Xiaobo; University of Missouri - Kansas City, Chemistry

Journal Name

ARTICLE

Two-Dimensional SnS_2 Nanosheets Exfoliated from Inorganic-Organic Hybrid with Enhanced Photocatalytic Activity towards Cr(VI) Reduction

Received 00th January 20xx,
Accepted 00th January 20xx

DOI: 10.1039/x0xx00000x

www.rsc.org/

Yongping Liu[a,b], Xihong Mi[a], Jixiang Wang[a], Ming Li[a], Dayong Fan[a*], Huidan Lu[a,b,*] and Xiaobo Chen[b*]

Atomic-scale thin two-dimensional materials have promising application prospect in photocatalysis due to their large reactive sites, short carrier diffusion distances and high charge separation properties. In this paper, SnS_2 nanosheets of several atomic layer thickness and dominating {001} facets are prepared with the liquid-exfoliation method using a SnS_2/n-propylamine inorganic-organic hybrid precursor. They become semi-metallic when the thickness is reduced to 30 Å, possess effective charge separation due to much shorter diffusion length in [001] direction as evidence from the prolonged photoluminescence lifetime, and exhibit largely improved photocatalytic activity for Cr (VI) reduction under the visible light irradiation, with a rate constant six-fold larger that of bulk SnS_2.

Introduction

Photocatalytic method, due to its environmentally friendly and economically advantages, is considered a green technology for the degradation of environmental pollutants[1]. Large optical absorption, adequate reactive sites, short carrier diffusion distances and high charge transport and separation properties are believed to be very important for effective photocatalysis [2-4]. SnS_2, an inexpensive, non-toxic, and relatively stable material with a peculiar CdI_2-type layered structure consisting of a S-Sn-S triple layer [5, 6], has a narrow band gap of 1.91 ~ 2.4 eV and has been studied as a promising semiconductor for photocatalytic water splitting[7] and CO_2 reduction[8], photoelectrochemical water splitting[9], chemical sensing[10], photodetectors[11], etc. Cr(VI) ions are frequently reported in our daily drinking water resources. They are highly toxic and induce various severe diseases such as bladder, skin, kidney and liver cancers [12]. It is therefore important to remove Cr(VI) ions from various environments[13]. SnS_2 nanoflowers and nanoyarns have been found with good activity for photoreduction Cr(VI) ions in waste water[14], and efficiency can be improved by constructing various heterostructures such as SnS_2/SnO_2[15]. However, low efficiency is commonly observed due to the poor charge transport and low separation rate of photogenerated electrons and holes in SnS_2[16, 17]. Thus, it is critical to develop ways in overcome such problems in order to use SnS_2 for that application.

Two-dimensional (2D) materials own many desirable merits for photocatalysis, potentially with one dominating high-energy facets, large surface areas, short carrier diffusion distances and high charge separation properties [18]. Those expected advantages have been observed in many semiconductor photocatalysis, such as $BiVO_4$[19], CdS[20], C_3N_4[21, 22], SnX_2 (X = S, Se)[6, 23], BiOI[24] and BiOBr[25].

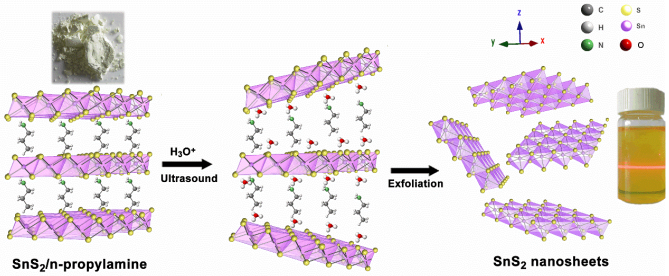

Scheme 1. A schematic illustration of the exfoliation of bulk SnS_2/n-propylamine into few-layer SnS_2 nanosheets, hydrogen atoms are omitted for clarity.

In this paper, thin SnS_2 nanosheets are prepared with a liquid-exfoliation method from a SnS_2/n-propylamine inorganic-organic hybrid precursor, as illustrated in Scheme 1. In general, 2D materials can be obtained through the exfoliation of inorganic-organic hybrids that are composed of few or single-layered inorganic targeting slabs sandwiched by the single-layer organic molecule via coordinated bonds[26-28]. The inserting organic molecule can be removed by ion exchange method[29, 30]. For this study, a bulk SnS_2/n-propylamine inorganic-organic hybrid is prepared first and then exfoliated into 2D SnS_2 in diluted nitric acid solution. Thin SnS_2 nanosheets are obtained with a thickness of 3.1 nm. The short thickness allows effective

[a] Guangxi Key Laboratory of Electrochemical and Magneto-chemical Functional Materials, College of Chemistry and Bioengineering, Guilin University of Technology, Guilin, 541004, China.
[b] Department of Chemistry, University of Missouri – Kansas City, Kansas City, Missouri 64110, United States
[c] Address here.
*Corresponding author: dyfan@glut.edu.cn (Dayong Fan), lhuidangl@163.com (Huidan Lu), chenxiaobo@umkc.edu (Xiaobo Chen)
Electronic Supplementary Information (ESI) available: [details of any supplementary information available should be included here]. See DOI: 10.1039/x0xx00000x

charge separation across the nanosheets, and increases the photocatalytic activity for Cr (VI) ion reduction.

Results and discussion

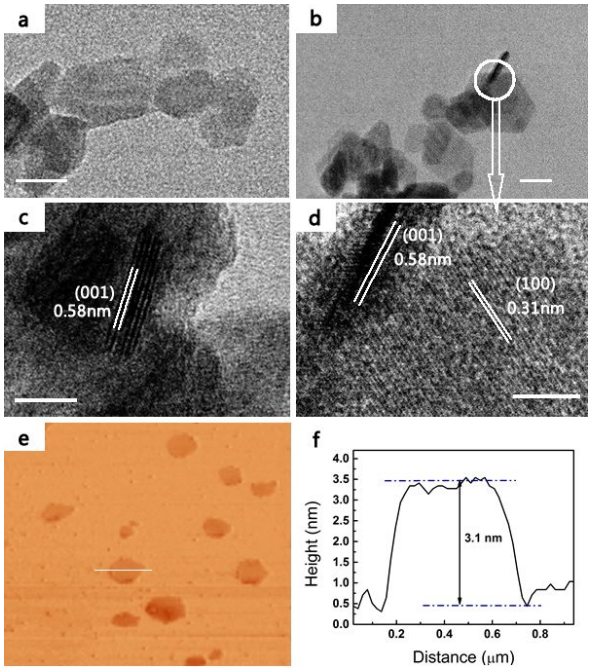

Fig. 1. TEM (a, b), HRTEM (c, d) images, AFM image(e) and the corresponding height profile(f) for SnS_2 nanosheets. The scale bars are 50 nm in (a, b), and 10 nm in (c, d).

SnS_2 nanosheets with {001} facet and 20 ~ 100 nm width were obtained as shown in Fig. 1 a and b after exfoliating the SnS_2/n-propylamine hybrid precursor of a nanosheet morphology (Fig. S1). The lattice spacing of 5.8 Å in the HRTEM image shown in Fig. 1c was indexed to the orientation-preferred (001) plane of SnS_2. The thickness of the large exfoliated SnS_2 nanosheets was about 3.1 nm based on the height profile of the AFM image shown in Fig. 1e and f. SnS_2 nanosheets were successfully obtained from the SnS_2/n-propylamine hybrid using most of the proton acid, such as acetic acid, H_2SO_4, HCl and HNO_3. Among them, the nitric acid had the highest efficiency. The SnS_2 nanosheet dispersion was stable over several days and showed a typical Tyndall effect (Fig. S2). In addition, thin WO_3 nanosheets (Fig. S3) were also obtained with the n-propylamine intercalation-exfoliation, indicating the potential wide applicability of this method in producing 2D materials.

The prepared bulk SnS_2 had a XRD pattern well matching the typical diffraction peaks of the 2T-type hexagonal SnS_2 (JPCDS, 83-1706) with the interlamellar spacing d = 5.86 Å (Fig. 2). SnS_2 nanosheets had much weaker but similar typical diffraction peaks compared to bulk SnS_2. The interlamellar spacing shifted to d = 5.78 Å based on the diffraction peak at 15.3°. The SnS_2/n-propylamine hybrid had a strong diffraction peak appears at $2\theta = 8.6°$ due to the insertion of n-propylamine between the SnS_2 layers [31, 32] and the interlamellar spacing d = 10.27 Å of the (001) facet of SnS_2/n-propylamine hybrid (Fig.S1). The disappearance of the diffraction peaks of the hybrid indicated that the n-propylamine has been eliminated from the formed nanosheets.

The infrared spectra of n-propylamine, SnS_2/n-propylamine and SnS_2 nanosheets were given in Fig. 2b. The SnS_2/n-propylamine hybrid had weaker vibration bands of $-CH_3$, $-CH_2$, and $-NH_2$ (curve 2) compared with pure n-propylamine (curve 3). Those vibration bands disappeared in SnS_2 nanosheets (#1) which had a broad band at 548 cm^{-1} from the Sn-S band vibration[33] and wide -OH vibration bands from the water adsorbed on the surface.

In the XPS spectra, nitrogen peak was only detected in the survey spectra of the SnS_2/n-propylamine hybrid (Fig. 3a), further showing that the SnS_2 nanosheets were fully exfoliated from the hybrid. The two main characteristic peaks of C 1s core-level spectra of the hybrid (Fig. 3b) were ascribed to the graphitic carbon (sp2 carbon ， 284.6 eV), C-NH_2 bonds (286.2 eV) [34]. The N 1s core-level of the hybrid had two peaks at 399.9 and 401.7 eV from the Sn-N [35] and C-NH_2 bonds[36], respectively, which were barely visible in SnS_2 nanosheets (Fig. 3c). The Sn $3d_{5/2}$ and $3d_{3/2}$ peaks in the hybrid were located at 486.5 eV and 494.9 eV[33, 37], lower than that in the SnS_2 nanosheets (Fig. 3d). Meanwhile, the S 2p peaks of the hybrid, reflecting to S-Sn bond[33, 37], shifted to lower energies (161.4 and 162.6 eV) than those in SnS_2 nanosheets (161.7 and 162.8 eV, Fig. 3e).

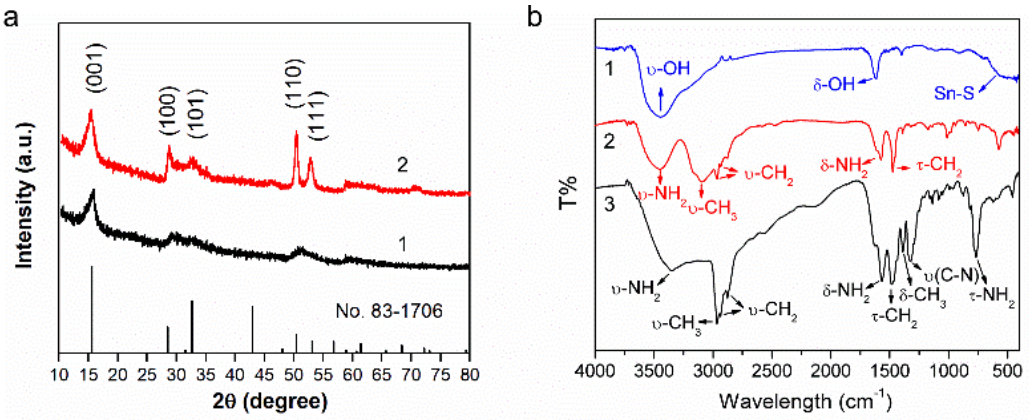

Fig. 2. (a) XRD patterns of (1) SnS_2 nanosheets and (2) bulk SnS_2, (b) FTIR spectra of (1) few-layer SnS_2 nanosheets, (2) bulk SnS_2/n-propylamine, and (3) n-propylamine.

Journal Name

ARTICLE

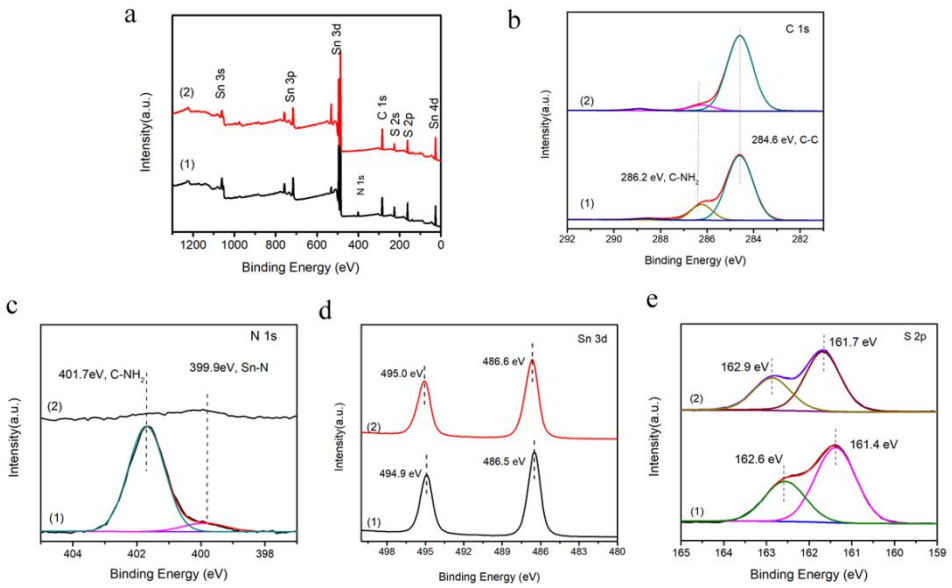

Fig. 3. XPS spectra of the as-synthesized samples: (a) the survey spectrum, (b) the high resolution of C 1s, (c) N 1s, (d) Sn 3d and (e) S 2p spectra. (1) SnS_2/n-propylamine, (2) SnS_2 nanosheets. (Replot all the graphs: all the graphs should have the same size and should be plotted from high energy to low energy (b-e).)

The decrease of the binding energy between Sn with S in the hybrid was due to the formation of Sn-N bond between n-propylamine in SnS_2 layers. These results confirmed that n-propylamine combined well with the bulk SnS_2 via Sn-N chemical bonds and exfoliation in diluted acid solution effectively remove n-propylamine between layers in forming SnS_2 nanosheets.

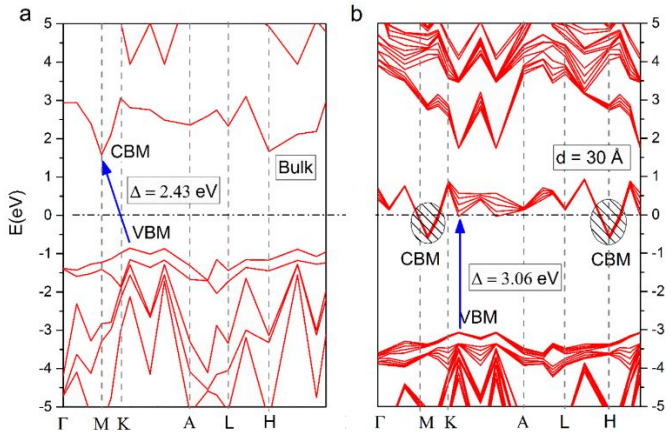

Fig. 4. Band structures calculated from first-principles density functional theory (DFT) for bulk (a) and SnS_2 nanosheet (b) with the thickness = 30 Å (b) along [001] direction. The Fermi level was set at E = 0 eV.

We calculated the electronic property of SnS_2 (beyond geometry) using the Heyd-Scuseria-Ernzerhof (HSE06) hybrid density functional [38]. Indirect to direct bandgap transition may occur when transition metal dichalcogenides undergo a change from bulk to a quasi 2D state [39]. As shown in Fig. 4, when the thickness of SnS_2 nanosheets in [001] direction was reduced to 30 Å, both the conduction and valence bands moved downward (Fig. 4), along with the valence-band maxima (VBM) located close to K. The CBM of SnS_2 nanosheets was below the fermi level (shadow region), showing semi-metallic state from semiconductor, consistent with the recent prediction of bilayer SnS_2 under a sufficient perpendicular electrical field [40]. The occupancy in conduction band intensely reduced the transition probability from VBM to CBMs, resulting in a vertical direct transition at CBM that became the main optical band gap, with the value increased from 2.43 eV to 3.06 eV. This was consistent with the optical bandgap based on the UV-vis measurements and the observed fluorescence results in the following section.

The optical absorption properties of bulk SnS_2, SnS_2/n-propylamine hybrid, and few-layer SnS_2 nanosheets were shown in Fig. 5. The SnS_2/n-propylamine hybrid only absorbed below ~450 nm, due to intercalation of n-propylamine. However, bulk SnS_2 and SnS_2 nanosheets displayed a wide absorption in the visible light region, where SnS_2 nanosheets absorbed much less than bulk SnS_2. The optical band gaps

estimated from the UV-vis diffuse reflection spectra were 2.13 eV for bulk SnS_2 and 2.35 eV for SnS_2 nanosheets, as shown in Fig. 5(b), consistent with those in the literature (1.91-2.35 eV) [33, 37 41, 42]. The larger band gap of SnS_2 nanosheets was likely due to the quantum confinement effects occurring on the (001) orientation of the SnS_2 nanosheets with 3.1 nm thickness, consistent with the DFT calculation results. As the layer thickness decreases, the extent of quantum confinement effect increases, as does the blue shift in their band-edge absorption. When n-propylamine intercalated between lays of SnS_2, similarly to SnS_2 single layer dispersed in n-propylamine, hybrid has the strongest quantum confinement effect. Thus, SnS_2/n-propylamine hybrid had a largest band gap of 3.05 eV. The similar results of large blue shift of their band-edge absorption were found in the hybrid of ZnS(butylamine)[43] , ZnSe(butylamine)[26], and ZnS(ethylenediamine)$_{0.5}$[44].

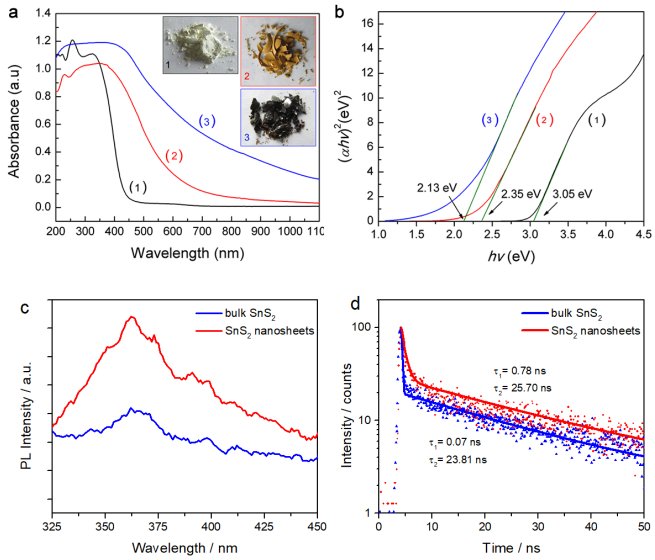

Fig. 5. (a) UV-vis diffuse reflectance spectra and (b) bandgap energies of (1) SnS_2/n-propylamine hybrid, (2) SnS_2 nanosheets, and (3) bulk SnS_2, (c) steady-state and (d) time-resolved PL of bulk SnS_2 (blue) and SnS_2 nanosheets (red) at room temperature.

TABLE 1. Decay times measured around the PL peak from time-resolved PL for bulk and nanosheet SnS_2 at room temperature.

SnS_2	τ_1(ns)	τ_2(ns)	β_1(%)	β_2(%)	χ^2
bulk	0.07	23.81	12.2	87.8	2.2
nanosheets	0.78	25.70	11.2	88.2	1.3

Some literatures reported that SnS_2 had a PL peak at 360 nm [45], others observed weak PL peak (due to the indirect bandgap nature of SnS_2) near optical bandgap at 550 nm, with single exponential decay (0.25-3.0) ns [46]. Here both bulk SnS_2 and nanosheets only showed PL peaks around 360 nm, as shown in Fig. 5c. The peak energy was located at 3.4 eV, likely reflecting the recombination of the electrons in the higher-lying conduction band with the holes in valence band. Compare to the bulk, SnS_2 nanosheets enhanced the PL intensity by a factor of 4. As the PL intensity was proportional to the corresponding density of excited states (DOEs). With the decrease of semiconductor dimension, the high-lying DOEs grew remarkably and showed much stronger optical absorption, due to the quantum confinement effect in [001] direction. The time-resolved PL showed that both bulk SnS_2 and nanosheets (Fig. 5d) had bi-exponential decays with the fast component (τ_1) and the slow component (τ_2). For the SnS_2 nanosheets, the fast component decay time (τ_1) was 0.78 ns, a 11-fold increase compared to the bulk, while the slow decay time (τ_2) appeared unchanged. The prolonged lifetime indicated the effective charge separation in SnS_2 nanosheets, likely due to the much shorter diffusion length in [001] direction.

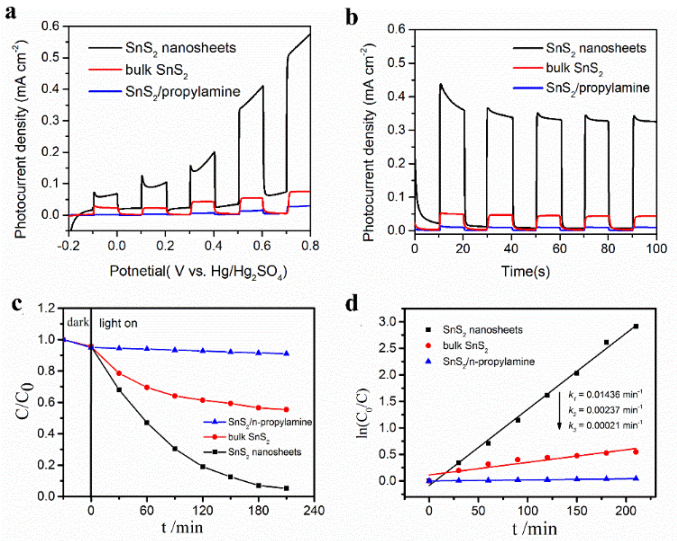

Fig. 6. The PEC performance of SnS_2 nanosheets, bulk SnS_2, SnS_2/n-propylamine hybrid, (a) linear sweep voltammograms from -0.2 – 0.8 V vs. Hg/Hg_2SO_4, (b) chronoamperometry at 0.6 V vs. Hg/Hg_2SO_4, (c) Photocatalytic reduction and (d)kinetic linear simulation curves of 100 mg/L Cr(VI) with (1) bulk SnS_2/n-propylamine hybrid, (2) bulk SnS_2, (3) SnS_2 nanosheets.

Fig. 6 showed PEC performance under dark and sunlight irradiation. SnS_2 nanosheets film displayed the photocurrent density of 0.4 mA/cm^2 at 0.6 V, about 10 and 40 times of the bulk SnS_2 (0.04 mA/cm^2) and the bulk SnS_2/n-propylamine hybrid (0.01 mA/cm^2), respectively. The enhancement was likely from the efficient transport and separation of photogenerated carriers in SnS_2 nanosheets. All the photocurrent density-time (i-t) curves displayed a good stability during the 100 seconds test (Fig. 6b).

The photocatalytic activity was evaluated through photocatalytic reduction conversion of Cr(VI) under visible light irradiation without using a sacrificial reagent. As shown in Fig. 6c, SnS_2 nanosheets (S_{BET}=64.3 m^{2}g^{-1}) had the highest photocatalytic activity with 96.5% Cr(VI) reduction within 210 min, followed by bulk SnS_2(S_{BET}=9.8 m^{2}g^{-1}) with ~48.3% Cr(VI) reduction, and bulk SnS_2/n-propylamine hybrid with only reduced ~5.9% Cr(VI) reduction. The kinetic analyses shown in Fig. 6d indicated that the Cr(VI) reduction was through a pseudo-first-order reaction model [47, 48], seen from the good

linear relationships between ln (C_0/C) and time. The rate constant of SnS_2 nanosheets (K_1 = 0.01436 min^{-1}) was about 6-fold bigger than that of bulk SnS_2 (K_2 = 0.00237 min^{-1}), showing a superior photocatalytic performance in Cr (IV) reduction. We also found that the ability of photocatalytic degradation of methyl orange by SnS_2 nanosheets was significantly improved. As shown in Figure S6, the rate constant of few-layers SnS_2 nanosheets (K_c = 0.1337 min^{-1}) is about 4.4 times of bulk SnS_2 (K_b = 0.0302 min^{-1}). We compare the photocatalytic reduction of hexavalent chromium using SnS_2 as photocatalysts in literatures. A brief summary lies in the Table S1 and illustrates in the Fig. S7. It is observed the atomic-scale thin SnS_2 nanosheets prepared in this work have the highest photocatalytic activity in the reported SnS_2 for Cr (VI) reduction. Their high specific areas, and quantum confinement effects within the several-nanometers-thick sheets could offer a much more active site and enhance the efficiency of the electron–hole separation in [001] direction, hence SnS_2 nanosheets have sharp performance in catalytic activity.

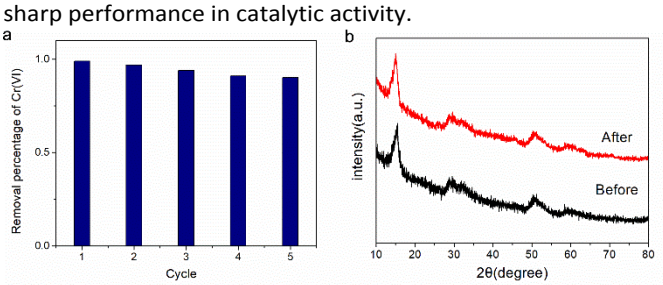

Fig. 7 (a) Recycling experiment for photocatalytic reduction of Cr(VI) in presence of the SnS_2 nanosheets and (b) XRD pattern of the SnS_2 nanosheets before and after five recycling experiment.

The recyclability of SnS_2 nanosheets for reduction of Cr (VI) were investigated (Fig. 7a). After 5 cycles, the photocatalytic efficiency of Cr (VI) reduction of SnS_2 nanosheet was maintained at 90%, and the XRD pattern (Fig. S7b) shows no significant change, indicating SnS_2 nanosheets has good reusability and structural stability for Cr (VI) photocatalytic reduction.

The mechanism of photocatalytic reduction of Cr (VI) by SnS_2 nanosheets is similar to by TiO_2 semiconductor[49], but they are a little different. As for TiO_2, two reaction of O_2 photoreduction and Cr (VI) photoreduction would occur simultaneously for the conduction band of TiO_2 (-0.43 V vs. NHE) is more negative than $E(O_2/\cdot O_{2-})$ (-0.33 V vs. NHE) and $E(Cr^{6+}/Cr^{3+})$ = 0.55 V (vs. NHE), respectively[50, 51]. While, the conduction band of SnS_2 is -0.32V (vs. NHE)[52], which is between $E(O_2/\cdot O_{2-})$ and $E(Cr^{6+}/Cr^{3+})$. Thus, under the illumination, the photogenerated electrons on SnS_2 surface do not have enough ability to reducing O_2, it directly combined with Cr(VI) to produce Cr(III). So, the mechanism of photocatalytic reduction of Cr (VI) in SnS_2 nanosheet is proposed as follows. At first electron–hole pairs produced in photocatalyst under illumination (eq. 1). Subsequently, the electrons and holes migrate to the surface of the SnS_2 nanosheets in [001] direction to participate in redox reactions. Holes take part in the reaction of the oxidation of H_2O (eq. (2) and H^+ is generated. Meanwhile, electrons can directly reduce Cr(VI) to Cr(III) (eq. (3).

$$SnS_2 + h\nu \rightarrow e^- + h^+ \quad (1)$$

$$H_2O + 2h^+ \rightarrow 1/2O_2 + 2H^+ \quad (2)$$

$$CrO_4^{2-} + 8H^+ + 3e^- \rightarrow Cr^{3+} + 4H_2O \quad (3)$$

Conclusions

In summary, SnS_2 nanosheets with exposing {001} facets and approximately 3.1 nm thick are synthesized with the liquid-exfoliation method from a bulk SnS_2/n-propylamine hybrid precursor. They exhibit superior photocatalytic activity in reduction of Cr(VI) compared to bulk SnS_2, likely due to the effective charge separation. Meanwhile, this work demonstrates a promising solution-based approach for developing 2D materials with very small thickness.

Experimental

Bulk SnS_2/n-propylamine hybrid material was synthesized by solvothermal method. $SnCl_4{\cdot}5H_2O$ (1 mmol), thioacetamide (4 mmol) and n-propylamine (16 mL) were added into a 40 mL Teflon-lined stainless-steel autoclave and reacted at 160 °C for 2 days. After the reaction, the autoclave was cooled to room temperature naturally. The white precipitates were collected by centrifugation, washed with distilled water and absolute ethanol several times, and finally dried in vacuum overnight.

25 mg SnS_2/n-propylamine hybrid was dispersed in 10 mL 3 M HNO_3, and sonicated in an ice-water bath for 1 h to obtain a yellow suspension, which was centrifuged to collect the precipitates that was then washed with distilled water, absolute ethanol for several times, in order to completely remove the HNO_3. Subsequently, the yellow precipitates were dispersed in absolute ethanol, sonicated for 5 min, and centrifuged at 1000 rpm for 10 min. The supernatant was finally collected by pipette and centrifuged at 8000 rpm for 15 min. Finally, SnS_2 nanosheets were collected after centrifuging the supernatant and drying in vacuum oven at 60 °C for 24h.

For a comparison, bulk SnS_2 was synthesized based on an established procedure[53]. Briefly, 2 mmol $SnCl_4{\cdot}5H_2O$ and 15 mmol thioacetamide were mixed in 40 mL distilled water, reacted in a 75mL Teflon-lined stainless-steel autoclave at 160 °C for 12 h.

The crystal structure was characterized with X-ray diffraction (XRD, PANalytical X'Pert PRO) with Cu Kα radiation (λ = 1.5418 Å). The microstructures were examined with transmission electron microscopy (TEM, JEOL, JEM-2100F), and atomic force microscopy (AFM, NT-MDT, Ntegra Prima SPM). Thermogravimetric analysis (TGA) was performed on a simultaneous thermal analysis (Waters (TA), SDF-Q600), where the SnS_2/n-propylamine hybrid was loaded into a platinum pan and heated with a ramp rate of 10 °C/min from room temperature to 800 °C in nitrogen atmosphere. Infrared spectra were taken using a Fourier transform infrared spectroscopy (Nicolet iS10, Thermo Fisher), diffuse reflectance spectra (DRS) using UV-VIS spectrometer (PE, Lambda 750) with $BaSO_4$ as the reference, and X-ray photoelectron spectroscopy (XPS) using a Thermo Electron ESCALAB 250Xi system. The Brunauer-

Emmett-Teller (BET) specific surface area was measured by nitrogen adsorption with Quantachrome Nova 1200. Steady-state photoluminescence (PL) spectra were measured on a spectrofluorophotometer (RF-5301PC, Shimadzu Corp). PL lifetime using a picosecond time-resolved fluorescence spectrometer, where the excitation wavelength was produced from an optical parametric amplifier (OPA-800-CF, Spectra Physics) pumped by a regenerative amplifier (800 nm, ~ 126 fs, Spitfire, Spectra Physics), a photon counting camera (Hamamatsu Photonics， C5680) was equipped for photon detection, the excitation energy was about 100 nJ / pulse, and the samples were spin-dropped on the indium tin oxide (ITO) glasses (1 cm × 1 cm). All the PL tests were performed at room temperature.

Photoanodes were fabricated as follows. The samples were dispersed in 5 mL ethanol (0.5 mg/mL), spin-dropped on the 1 cm × 1 cm indium tin oxides (ITO) glass at 600 rpm for 30 s, and heated at 60 °C for 1 h. The photoelectrochemical (PEC) tests were conducted in a conventional three-electrode system with an electrochemical workstation (CHI860) under irradiation of 590 W Xe lamp (Oriel instrument, 91192-1000, Newport), where the potential swept rate was set to 10 mV/s, 0.5 M Na_2SO_4 solution, platinum wire and saturated Hg/Hg_2SO_4 electrode as the electrolyte, counter and reference electrodes, respectively.

The photocatalytic reduction of aqueous Cr (VI) ions (50 mg/L) was conducted under a 300 W Xe lamp irradiation (PLS-SEX300, Perfect Light, λ>420 nm). 50 mg catalysts were suspended in a glass flask (200 mL) containing 100 mL $K_2Cr_2O_7$ aqueous solution. Before illumination, the suspensions were stirred for 30 min in the dark to ensure establishment of Cr (VI) adsorption equilibrium. The concentration of the Cr(VI) concentration was determined with the diphenylcarbazide colorimetric method [54].

Conflicts of interest

There are no conflicts to declare.

Acknowledgements

This work was supported by the National Natural Science Foundation of China (21363006, and 21503051), Natural Science Foundation of Guangxi Province (2016GXNSFAA380121, 2016GXNSFAA380219, 2018GXNSFAA138108), X. C. appreciates the support from the U.S. National Science Foundation (DMR-1609061), and the College of Arts and Sciences, University of Missouri-Kansas City

Notes and references

1. J. Low, J. Yu, M. Jaroniec, S. Wageh and A. A. Al-Ghamdi, *Adv. Mater.*, 2017, **29**, 1601694.
2. Y. Ma, X. Wang, Y. Jia, X. Chen, H. Han and C. Li, *Chem. Rev.*, 2014, **114**, 9987-10043.
3. J. Wen, J. Xie, X. Chen and X. Li, *Appl. Surf. Sci.*, 2017, **391**, 72-123.
4. L. Guan and X. Chen, *ACS Applied Energy Materials*, 2018, **1**, 4313-4320.
5. Y. Sun, H. Cheng, S. Gao, Z. Sun, Q. Liu, Q. Liu, F. Lei, T. Yao, J. He, S. Wei and Y. Xie, *Angew. Chem. Int. Edit.*, 2012, **51**, 8727-8731.
6. Y. Liu, P. Geng, J. Wang, Z. Yang, H. Lu, J. Hai, Z. Lu, D. Fan and M. Li, *J. Colloid Interf. Sci*, 2018, **512**, 784-791.
7. C. Yan, X. Xue, W. Zhang, X. Li, J. Liu, S. Yang, Y. Hu, R. Chen, Y. Yan, G. Zhu, Z. Kang, D. J. Kang, J. Liu and Z. Jin, *Nano Energy*, 2017, **39**, 539-545.
8. I. Shown, S. Samireddi, Y. C. Chang, R. Putikam, P. H. Chang, A. Sabbah, F. Y. Fu, W. F. Chen, C. I. Wu, T. Y. Yu, P. W. Chung, M. C. Lin, L. C. Chen and K. H. Chen, *Nat. Commun.*, 2018, **9**, 169.
9. G. B. Liu, Z. H. Li, T. Hasan, X. S. Chen, W. Zheng, W. Feng, D. C. Jia, Y. Zhou and P. A. Hu, *J. Mater. Chem. A*, 2017, **5**, 1989-1995.
10. C. Kim, J. C. Park, S. Y. Choi, Y. Kim, S. Y. Seo, T. E. Park, S. H. Kwon, B. Cho and J. H. Ahn, *Small*, 2018, **14**, e1704116.
11. Y. Hu, T. Chen, X. Wang, L. Ma, R. Chen, H. Zhu, X. Yuan, C. Yan, G. Zhu, H. Lv, J. Liang, Z. Jin and J. Liu, *Nano Research*, 2017, **10**, 1434-1447.
12. A. K. Nayak, S. Lee, Y. I. Choi, H. J. Yoon, Y. Sohn and D. Pradhan, *ACS Sustainable Chemistry & Engineering*, 2017, **5**, 2741-2750.
13. F. Xu, H. Chen, C. Xu, D. Wu, Z. Gao, Q. Zhang and K. Jiang, *Journal of colloid and interface science*, 2018, **525**, 97-106.
14. C. Mondal, M. Ganguly, J. Pal, A. Roy, J. Jana and T. Pal, *Langmuir.*, 2014, **30**, 4157-4164.
15. L. Ma, L. Xu, X. Xu, L. Zhang and X. Zhou, *Ceramics International*, 2016, **42**, 5068-5074.
16. J. Liu, K. He, W. Wu, T. B. Song and M. G. Kanatzidis, *J. Am. Chem. Soc.*, 2017, **139**, 2900-2903.
17. G. M. Kumar, F. Xiao, P. Ilanchezhiyan, S. Yuldashev and T. W. Kang, *RSC Adv.*, 2016, **6**, 99631-99637.
18. J. Di, J. Xia, H. Li and Z. Liu, *Nano Energy*, 2017, **35**, 79-91.
19. D. C. L. Zhang, X. Jiao,, *Chem.B*, 2006, **110**, 2668-2673.
20. C. Bie, J. Fu, B. Cheng and L. Zhang, *Applied Surface Science*, 2018, **462**, 606-614.
21. X. Zhang, X. Xie, H. Wang, J. Zhang, B. Pan and Y. Xie, *Journal of the American Chemical Society*, 2012, **135**, 18-21.
22. Y. P. Liu, P. Chen, Y. Chen, H. D. Lu, J. X. Wang, Z. S. Yang, Z. H. Lu, M. Li and L. Fang, *RSC Adv.*, 2016, **6**, 10802-10809.
23. J.-J. Wu, Y.-R. Tao, X.-C. Wu and Y. Chun, *Journal of Alloys and Compounds*, 2017, **713**, 38-45.
24. L.-w. Shan, L.-q. He, J. Suriyaprakash and L.-x. Yang, *Journal of Alloys and Compounds*, 2016, **665**, 158-164.
25. Z. Cui, H. Song, S. Ge, W. He and Y. Liu, *Applied Surface Science*, 2019, **467-468**, 505-513.
26. J. L. X. Huang, J. , *J. Am. Chem. Soc.* , 2007, **129** 3157-3162.
27. H. B. Yao, X. Zhang, X. H. Wang, S. H. Yu and J. Li, *Dalton transactions*, 2011, **40**, 3191-3197.
28. S. Wang and J. Li, *Journal of Solid State Chemistry*, 2015, **224**, 40-44.
29. L. Liang, J. Zhang, Y. Zhou, J. Xie, X. Zhang, M. Guan, B. Pan and Y. Xie, *Scientific reports*, 2013, **3**, 1936.
30. W. T. Yao, S. H. Yu and Q. S. Wu, *Advanced Functional Materials*, 2007, **17**, 623-631.
31. G. A. O. T. Jiang, . *J. Mater. Chem.* , 1997, **7**, 2213-2222.
32. H. K. J.Q. Li, L. Delmotte., *J. Chem. Soc.Faraday Trans.*, 1997, **93**, 665-668.
33. Z. Zhang, C. Shao, X. Li, Y. Sun, M. Zhang, J. Mu, P. Zhang, Z. Guo and Y. Liu, *Nanoscale*, 2013, **5**, 606-618.
34. T. H. A.D. Vogt, T.P. Beebe., *Langmuir*, 1997, **13**, 3397-3403.

35. B. Zhou, S. Dong, H. Zhao, Y. Liu and P. Wu, *Journal of Magnetism and Magnetic Materials*, 2014, **362**, 14-19.
36. S.-W. Cao, X.-F. Liu, Y.-P. Yuan, Z.-Y. Zhang, Y.-S. Liao, J. Fang, S. C. J. Loo, T. C. Sum and C. Xue, *Applied Catalysis B: Environmental*, 2014, **147**, 940-946.
37. Y. C. Zhang, Z. N. Du, K. W. Li, M. Zhang and D. D. Dionysiou, *ACS applied materials & interfaces*, 2011, **3**, 1528-1537.
38. J. Heyd, G. E. Scuseria and M. Ernzerhof, *The Journal of Chemical Physics*, 2003, **118**, 8207-8215.
39. Q. H. Wang, K. Kalantar-Zadeh, A. Kis, J. N. Coleman and M. S. Strano, *Nature nanotechnology*, 2012, **7**, 699-712.
40. C. Bacaksiz, S. Cahangirov, A. Rubio, R. T. Senger, F. M. Peeters and H. Sahin, *Physical Review B*, 2016, **93**.
41. Y. C. Zhang, Z. N. Du, S. Y. Li and M. Zhang, *Applied Catalysis B: Environmental*, 2010, **95**, 153-159.
42. C. Yang, W. Wang, Z. Shan and F. Huang, *Journal of Solid State Chemistry*, 2009, **182**, 807-812.
43. G. Zhu, J. Yang, C. Bao, X. Zhang, Z. Ji, S. Wu and X. Shen, *Journal of colloid and interface science*, 2016, **468**, 136-144.
44. A. Hernández-Gordillo, F. Tzompantzi and R. Gómez, *international journal of hydrogen energy*, 2012, **37**, 17002-17008.
45. K. T. C. Wang, Q. Yang, Y. Qian., *Chem. Phys. Lett.*, 2002, **357**, 371-375.
46. Y. B. Yang, J. K. Dash, A. J. Littlejohn, Y. Xiang, Y. Wang, J. Shi, L. H. Zhang, K. Kisslinger, T. M. Lu and G. C. Wang, *Crystal Growth & Design*, 2016, **16**, 961-973.
47. D. F. O. C.S. Turchi, *J. Catal.*, 1990, **122**, 178.
48. M. S. Lee, S. S. Park, G.-D. Lee, C.-S. Ju and S.-S. Hong, *Catalysis Today*, 2005, **101**, 283-290.
49. A. Giannakas, E. Seristatidou, Y. Deligiannakis and I. Konstantinou, *Applied Catalysis B: Environmental*, 2013, **132**, 460-468.
50. S. Fan, X. Li, L. Zeng, M. Zhang, Z. Yin, T. Lian and A. Chen, *ACS applied materials & interfaces*, 2018, **10**, 35919-35931.
51. S. Fan, X. Li, Q. Zhao, L. Zeng, M. Zhang, Z. Yin, T. Lian, M. O. Tadé and S. Liu, *Dalton transactions*, 2018, **47**, 12769-12782.
52. J. Lin, Y. Liu, Y. Liu, C. Huang, W. Liu, X. Mi, D. Fan, F. Fan, H. Lu and X. Chen, *ChemSusChem*, **0**.
53. H. C. S Y. Sun, S. Gao, Z. Sun, Q. Liu, Q. Liu, F. Lei, T. Yao, J. He, S. Wei, Y. Xie., *Angew. Chem. Int. Ed.*, 2012, **51**, 8727-8731.
54. A. Idris, N. Hassan, R. Rashid and A. F. Ngomsik, *Journal of hazardous materials*, 2011, **186**, 629-635.